Physics–informed guided wave modes as robust identifiers of progressive structural degradation in thin–walled composite structures

Anirudh Gullapalli*, Carol Featherston † and Abhishek Kundu‡
School of Engineering, Queen's Buildings, 14-17 The Parade, Cardiff University, Cardiff CF24 3AA, United Kingdom

Ultrasonic guided waves hold significant potential for non-intrusive monitoring of progressive damage in composite structures, contingent on the efficacy of the onboard monitoring system to reliably acquire, process signals. By mapping the extracted signal features with parameterized damage metrics, it is possible to realize an automated framework for the assessment of structural integrity. It is well established that fundamental ultrasonic guided wave modes are sensitive to damage in laminated composite structures and can serve as robust damage identifiers when properly characterized. But there is a gap in understanding of the modified behavior in waveguide dispersion properties due to the presence of damages or deterioration of waveguide properties. Therefore, it is vital to establish a generic, extendable and reproducible wave mode reconstruction methodology so that the fundamental ultrasonic guided wave modes can be investigated for damage signatures. Towards this, The fundamental S_0 and A_0 modal amplitudes and dispersion characteristics were calibrated using a physics-informed harmonic wave propagation model. This process generated individual mode realizations that were then superimposed to produce accurate reconstructions of experimental signals acquired from a sparse array of piezoelectric transducers. A regularized residual error function was formulated to account for discrepancies from measurement noise, unmodeled higher-order modes, and other sources of error. A probabilistic Bayesian joint parameter estimation approach was employed to minimize this error and calibrate the wave mode characteristics. The calibrated parameters were subsequently used to investigate progressive structural degradation arising from displacement-controlled compressive fatigue loading. A probabilistic Bayesian joint parameter estimation framework effectively captured direction–specific signatures and quantified uncertainty in parameter estimation, revealing distinct directional and modal sensitivities to fatigue damage. This achievement underscores the efficacy and reliability of the calibrated ultrasonic guided wave modes as reliable identifiers of damage with potential for further description, characterization, and sentencing.

I. Nomenclature

SHM	=	Structural health monitoring
UGW	=	Ultrasonic guided wave
SAFE	=	Semi-analytical finite element
CFRC	=	Carbon fiber reinforced composite
RREF	=	Regularized residual error function
ToF	=	Time of flight
PSD	=	Power spectral density
R	=	Pearson correlation coefficient to quantitatively demonstrate experimental and reconstructed signal concordance.
S_0	=	Symmetric fundamental ultrasonic guided wave mode.
A_0	=	Antisymmetric fundamental ultrasonic guided wave mode.
SH_0	=	Shear–horizontal fundamental ultrasonic guided wave mode.
θ_p	=	Direction of guided wave propagation

*PhD student, School of Engineering, Cardiff University, gullapallias@cardiff.ac.uk
†Professor, School of Engineering, Cardiff University
‡Senior Lecturer, School of Engineering, Cardiff University, kundua2@cardiff.ac.uk

$\mathbf{r}$	=	Position vector from actuating transducer to sensing transducer, distance r (m), for a given $\theta(^\circ)$
t	=	time (s)
ω	=	Circular frequency (rad/s)
n_s	=	Number of sensing transducers bonded to the test structure.
n_ω	=	Number of harmonic components of signal within a chosen frequency window.
$g(\omega)$	=	The complex frequency response of the actuation signal and the system transfer function.
$U_m(r,t)\big\rvert_{\theta_p}$	=	Lamb wave propagating in a plate like structure as a function of r and t along θ_p
U_{S_0}	=	Symmetric S_0 guided wave mode amplitude
U_{A_0}	=	Antisymmetric A_0 guided wave mode amplitude
$\vec{k}_{S_{0,\theta_p}}$	=	S_0 mode wave number along θ_p direction (m^{-1})
$\vec{k}_{A_{0,\theta_p}}$	=	A_0 mode wave number along θ_p direction (m^{-1})
$V_{P_{\mathrm{S}_0}}$	=	Phase velocity of S_0 mode, given by $\frac{\omega}{\boldsymbol{k}_{\mathrm{S}_0}}$ (m/sec)
$V_{P_{\mathrm{A}_0}}$	=	Phase velocity of A_0 mode, given by $\frac{\omega}{\boldsymbol{k}_{\mathrm{A}_0}}$ (m/sec)
$V_{G_{\mathrm{S}_0}}$	=	Group velocity of S_0 mode, given by $\frac{\partial\omega}{\partial\boldsymbol{k}_{\mathrm{S}_0}}$ (m/sec)
$V_{G_{\mathrm{A}_0}}$	=	Group velocity of A_0 mode, given by $\frac{\partial\omega}{\partial\boldsymbol{k}_{\mathrm{A}_0}}$ (m/sec)
Θ	=	Wave mode parameters calibrated in this study $[U_{S_0}, U_{A_0}, V_{P_{\mathrm{S}_0}}, V_{P_{\mathrm{A}_0}}, V_{G_{\mathrm{S}_0}}, V_{G_{\mathrm{A}_0}}]$
$H(x)(t)$	=	Hilbert envelope of the experimental structural-acoustic response.
$H(x^M)(t)$	=	Hilbert envelope of the reconstructed signal.
ε_H	=	Euclidean norm of the difference between the experimental and calibrated Hilbert analytic envelopes
ε_{V_P}	=	Euclidean norm of the difference between the semi-analytical and calibrated phase velocities
ε_{V_G}	=	Euclidean norm of the difference between the semi-analytical and calibrated group velocities

II. Introduction

Modern aerospace and automotive systems increasingly rely on multilayered composite materials to achieve optimal strength-to-weight ratios and performance under varying environmental and loading conditions. Throughout their lifecycle, these structures are susceptible to progressive degradation mechanisms such as interlaminar delaminations, [1], interfacial debonding [2] and fibre-breakage [3] amongst others. The damage may be initiated at the manufacturing stage due to imperfections such as porosity, impurities and fiber-misalignment [4, 5] or in service due to the action of tension, compression, torsion, impact and fatigue. Unlike isotropic materials, CFRCs exhibit complex damage progression patterns [6–10] that often evade conventional inspection methods, posing significant challenges for early damage onset detection and reliability assessment in safety critical engineering applications[11, 12]. Predictive maintenance holds great promise to operate within data-rich environments created by continuous monitoring regimes. However, the acquired dataset is not useful unless the essential features are extracted and mapped to certain behavioural patterns of the structure which may vary due to degradation. The identification and selection of these key features play a vital role in optimizing efficiency, improving detection performance and enabling practical predictive maintenance [13].

Most essential signal features can be divided into two groups – overall guided wave signal features and guided wave mode-specific features. The overall guided wave signal features provide damage indication while the guided wave mode–specific features provide damage information. Because the overall summary statistics are related to aggregated signal properties, there is usually a significant difficulty in relating these features to the underlying physics of the damage influencing the guided wave propagation behaviour. Furthermore, the uncertainty associated with these aggregated signal features and their changes makes it difficult to reproduce the proposed changes in a consistent fashion to the damage metrics. A list of the commonly used damage sensitive features for lamb waves [14] in structural health monitoring (SHM) is given in Table 2.

Studies have found that various wave modes have different interactions with various types of composite damage [15, 16]. For example, the S_0 mode was found to be sensitive to impact damage but not sensitive to the delamination simulated by the Teflon insert. On the other hand, the SH_0 mode was sensitive to both simulated delamination and impact damage [17]. The S_0 mode which is dominant at higher frequencies, caused mode conversions when interacting with the defects whereas A_0 mode, dominant at lower frequencies, mainly caused a change in phase and amplitude upon interaction with defects [18]. Consistent findings across studies showed amplitude reductions due to damage presence. Specifically, impact damage caused a strong amplitude decrease for the S_0 mode because impact damage, in the form of matrix cracking, fiber breakage, or interlaminar delamination, significantly reduced local material stiffness [19].

In addition to wave mode sensitivity to specific types of damage, studies demonstrated that guided wave modes can effectively detect and monitor fatigue damage evolution in composite structures. Specifically, the ToF, amplitude and PSD of the guided waves were sensitive to fatigue induced matrix cracks and delaminations [20].

Therefore, it can be inferred that amongst the commonly extracted essential signal features, most of them have direct and strong dependence on the knowledge of fundamental ultrasonic guided wave modes within the acquired ultrasonic responses. This makes the identification and isolation of fundamental ultrasonic guided wave modes the most crucial feature extraction operation that can be performed on the acquired structural ultrasonic responses. Reported methodologies for guided wave mode isolation can be primarily classified into pre–acquisition and post–acquisition paradigms, each presenting their own constraints. The first paradigm relies on hardware-based strategies applied before data acquisition, such as employing specialized transducers, prescribing specific actuation frequencies, or controlling actuator–sensor distances to preferentially excite a single mode. Although effective, these methods are experimentally rigid and the mode of interest must be selected a priori. Post–acquisition techniques operate by extracting wave packets based on time–of–arrival of their peaks. However, these methods are fundamentally heuristic and fail in identifying these peaks when wave modes overlap in the time and time-frequency domains [33–36]. Additionally, the principal shortcoming of these methods is their physics-agnostic nature; they treat the signal as raw data without incorporating the dispersion characteristics embodied in phase and group velocity curves that govern guided wave propagation.

There exists a lack of a robust, streamlined and reproducible physics–informed methodology for isolating guided wave modes to capture damage signatures. This study directly addresses this issue by calibrating and reconstructing experimental guided wave modes to establish them as reliable criteria for damage signature identification. The concept of physics-informed robust one-dimensional calibration of guided wave mode characteristics was first introduced in previous work [37], where the fundamental S_0 and A_0 modes were calibrated to generate accurate reconstructions of signals acquired using a linear transducer array along a single propagation direction on a thin-walled CFRC structure. In this paper, a two-dimensional calibration of S_0 and A_0 modes along different radial propagation directions, enabling accurate signal reconstruction at any angular position θ and distance r. Furthermore, the calibrated guided wave mode characteristics were utilized to capture structural degradation in the CFRC panel resulting from cyclic displacement–controlled compressive fatigue loading. This achievement underscores the reliability of the the reconstructed ultrasonic guided wave modes as digital damage identifiers for damage detection, characterization, and quantification. It is important to note that the results presented in this study showcase the efficacy of the calibrated wave mode characteristics in capturing progressive structural degradation. Mapping the captured signatures to parameterized damage metrics is the future scope of this research.

The remainder of this paper is structured as follows. section III outlines the experimental setup, data acquisition procedure, and wave mode calibration methodology employed to capture progressive structural degradation in a 12–layered CFRC panel under cyclic displacement-controlled compressive fatigue. section IV delineates the results obtained from the probabilistic Bayesian joint parameter estimation methodology, demonstrating how progressive degradation manifests in the calibrated wave mode characteristics and compares them with experimental measurements. Finally, section V summarizes the conclusions and highlights future directions.

Guided Wave Mode-Specific Features	
Essential Signal Feature	**Remarks**
Time-of-Flight (ToF) [21, 22]	When lamb waves interact with damage, mode conversion can occur consequently altering the propagation velocity and hence the ToF.
Peak-to-Peak Amplitude [23, 24]	The interaction of fundamental Lamb wave modes with the structural features or damage can also lead to mode-specific changes in amplitude. This can result in mode-dependent peak–to–peak amplitude variations that are useful for damage detection and characterization.
Attenuation [25, 26]	Mode-dependent (e.g., in plates, A_0 attenuates faster than S_0). Requires separation of modes to quantify accurately.
Scattering Coefficients [27, 28]	Governed by mode interaction with defects (e.g., symmetric vs. antisymmetric mode scattering patterns).
Wave Energy [25, 29]	Sum of individual modal energies. Reconstruction helps to isolate contributions from individual modes.
FFT Coefficients [30]	Peaks correspond to mode resonances, but overlapping modes complicate interpretation.
Power Spectral Density (PSD) [14]	Frequency-domain representation of signal energy; requires mode separation for accurate damage assessment.
Wavelet Coefficients [31, 32]	Provide a sensitive and robust method for capturing multiple aspects of damage-wave interactions across fundamental Lamb wave modes.
Overall Guided Wave Signal Features	
Essential Signal Feature	**Remarks**
Root Mean Square	Lumped metric with no mode-specific information.
Skewness	Sensitive to overall signal shape but agnostic to underlying modes.
Kurtosis	Compares the tailedness/peakedness of signal distribution relative to the normal distribution; not directly linked to wave modes.
Magnitude	Lumped metric with no mode-specific information.

Table 2 Commonly used essential signal features for damage description and their dependence on guided wave modes. The overall guided wave signal features provide damage indication while the guided wave mode–specific features provide damage information (location, severity etc.).

III. Materials and methods

This section begins by detailing the mechanical and geometric properties of the composite panel, the compressive fatigue test rig along with the loading parameters and the autonomous, ready-to-deploy, smart edge computing signal generation/reception framework utilized to acquire the ultrasonic responses from the CFRC panel in section III.A. Subsequently, the key components of the physics–informed calibration encompassing the harmonic wave propagation function ($\mathcal{M}$), the regularized residual error formulation (ε) and the probabilistic Bayesian joint parameter estimation regime are outlined in section III.B, section III.C and section III.D respectively.

A. Experimental section

The experimental setup consisted of a symmetric 12–layered CFRC panel of dimension $410 \times 380 \times 2.5$ mm, with a layup configuration of $[+45_3/-45_3]_S$ equipped with NANO30 transducers positioned in a semi-circular orientation of radius 100mm at angular positions of $0°, 45°, 90°, 135°, 180°$, as depicted in figure 1. A threshold-free ultrasonic guided wave–based active inspection framework termed *CyberSHM* was employed to acquire and process ultrasonic data collected form thin-walled plate-like structures in real-time. A smart–edge node, comprising a sparse array of NANO30 transducers and a daisy–chained edge computing device, excites thin–walled structures with user–defined frequency–swept actuation signals. The system acquires and processes ultrasonic structural responses using customized open-source Python scripts. Programmable edge-based tasks include file manipulation, signal feature extraction, classification, and data transmission to a digital layer for subsequent analysis. These integrated capabilities enable real–time, inspection of thin–walled plate–like structures using ultrasonic guided waves.

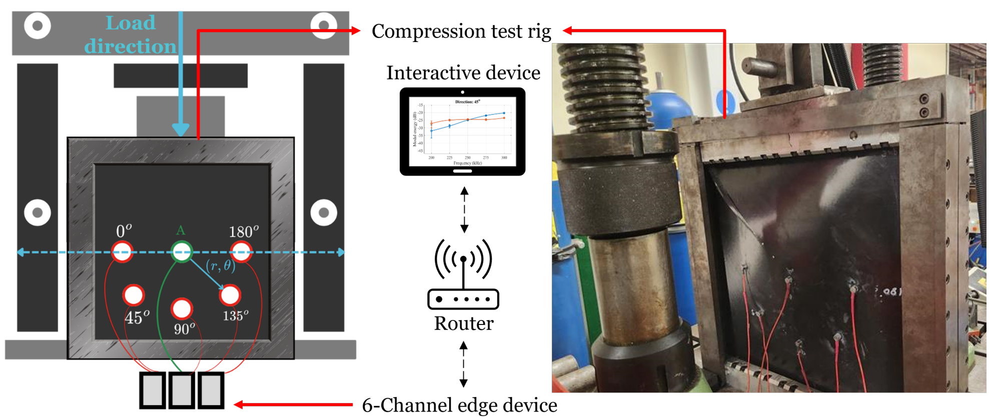

Fig. 1 Experimental setup: compressive fatigue testing apparatus, CFRC panel equipped with a semi-circular array of actuator A and five transducers used to acquire ultrasonic responses (actuator–transducer distance 100mm)

The smart–edge–node in this study incorporated three edge devices interconnected in a daisy-chain configuration, establishing a six-channel signal generation and reception system. The device excited the panel with a 10–cycle Hanning-windowed toneburst signal at 2V peak–to–peak amplitude coupled with a 100–factor gain while simultaneously acquiring guided wave responses. An in-line classification algorithm processed the captured time–domain signals in real–time, distinguishing between relevant acoustic–event–representative signatures and non–essential signals. Only waveforms identified as containing meaningful structural information were retained for subsequent wave mode calibration. The data acquisition and in–line classification capabilities of the smart–edge–node, were previously conceptualized, developed, and experimentally validated in our publication [38]. The digital layer incorporates a semi–analytical model that analyzes elastic wave dispersion in laminated composite waveguides, accurately capturing fundamental guided wave characteristics and simulating dispersion phenomena in composite materials.

The compressive test rig, shown in figure 1 , was designed to provide simple supports to all four sides of the specimens whilst facilitating the application of a uni–axial in–plane compressive load. The construction and assembly of the test rig are described in [39], where the rig was utilized to study buckling and failure in CFRCs for acoustic emission structural health monitoring.

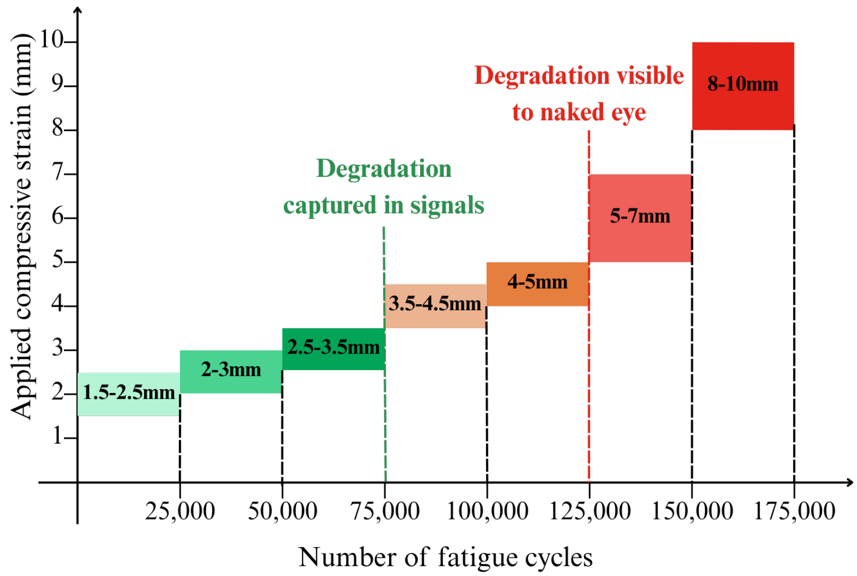

Fig. 2 Displacement control fatigue loading with gradual increments in the applied compressive strain.

In this study, the CFRC being investigated was subjected to displacement control compressive fatigue loading with the aim of capturing the progressive degradation in the calibrated wave mode characteristics. A total of $175,000$ cycles of fatigue were performed, acquiring the structural ultrasonic responses after every $25,000$ cycles and increasing the applied compressive strain in accordance with figure 2. Subsequently, the fundamental S_0 and A_0 mode characteristics were calibrated and accurate reconstructions of the acquired ultrasonic signals were generated.

B. Direction dependent harmonic wave propagation function ($\mathcal{M}$)

This concept was first formulated as a one–dimensional harmonic wave propagation function to calibrate wave modes along a single propagation direction [37]. However, the directional dependence of specific wave modes on the fibre orientation in the composite layup is crucial to achieve accurate reconstructions of experimental signals. Therefore, the modal amplitudes, direction dependent phase velocities and group velocities were chosen as parameters to calibrate.

$$\Theta = \{U_{S_0}, U_{A_0}, V_{P_{S_0}}, V_{P_{A_0}}, V_{G_{S_0}}, V_{G_{A_0}}\}$$

and hence, the direction dependent harmonic wave propagation function at a given frequency ω was formulated as,

$$U_m(\boldsymbol{r}, t; \omega) = U_{S_0} e^{j\left(\boldsymbol{k}_{S_0}^{\top}\boldsymbol{r} - \omega t\right)} + U_{A_0} e^{j\left(\boldsymbol{k}_{A_0}^{\top}\boldsymbol{r} - \omega t\right)} + \varepsilon \tag{1}$$

In equation 1, $\boldsymbol{r}$ denotes the position vector from the actuating transducer to the sensor, θ_p is the direction of propagation with respect to X–axis, ω is the angular frequency, t is the time, U_{S_0} and U_{A_0} are the amplitudes and $\boldsymbol{k}_{S_0}(\omega, \theta_p)$ and $\boldsymbol{k}_{A_0}(\omega, \theta_p)$ are the frequency and direction–dependent wavenumber vectors of the S_0 and A_0 modes respectively. Here ε denotes the residual error to account for measurement and prediction discrepancies. The two fundamental ultrasonic guided wave modes were modelled using the phase and group velocity values obtained from a semi-analytical model. Although the CFRC panel is excited by a toneburst sinusoidal ultrasonic signal at a specific center frequency $\omega = \omega_0$, the signal propagating through the material contains a distribution of frequencies within a bandwidth $\omega \pm \Delta\omega$. This spectral broadening arises from interactions between ultrasonic guided wave modes and the multilayered composite architecture. Consequently, the signal measured along a given propagation direction θ_p represents a superposition of wave components, modeled by the summation of equation 1 across the effective frequency band.

$$U_m(r, t)\Big|_{\theta_p} = \frac{1}{2\Delta\omega} \int_{\omega-\Delta\omega}^{\omega+\Delta\omega} \left[U_{S_0} e^{jk_{S_0,\theta_p} r} g(\omega) e^{-j\omega t} + U_{A_0} e^{jk_{A_0,\theta_p} r} g(\omega) e^{-j\omega t} \right] \mathrm{d}\omega \tag{2}$$

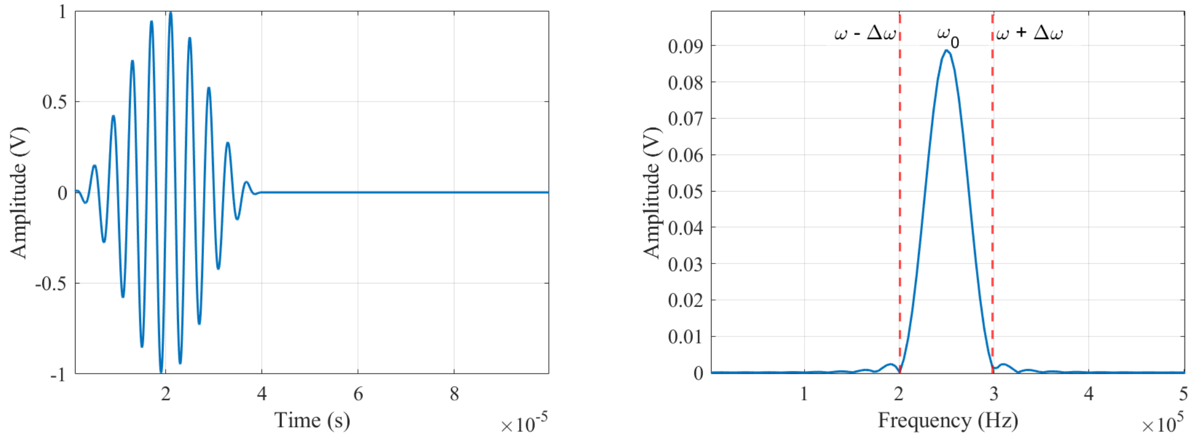

(a) **(b)**

Fig. 3 (a) $2V_{pp}$**,** 10 **period, Hanning-windowed toneburst actuation signal (b) Frequency response of the actuation signal**

Evaluating the integrals as a discrete summation over frequency step size $\delta\omega_i$, we have

$$\overline{U}_{S_0}(r,t)\Big|_{\theta_p} = \frac{U_{S_0}}{2\Delta\omega}\sum_i g(\omega_i)e^{j\vec{k}_{S_0,\theta_p}r-\omega_0 t}e^{jn\delta\omega_i\left(\frac{r}{V_{G_{S_0}}}-t\right)}\delta\omega_i \tag{3}$$

Considering there are n_ω harmonic components within a chosen frequency window, $\Delta\omega = n_\omega\delta\omega$. After certain algebraic manipulations, we arrive at the individual mathematical realizations of the S_0 and A_0 modes as follows:

$$\overline{U}_{S_0}(r,t)\Big|_{\theta_p} = \frac{U_{S_0}}{2n_\omega}e^{j\omega_0\left(\frac{r}{V_{P_{S_0}}}-t\right)}\left[\sum_{n=0}^{n_\omega} g(\omega+n\delta\omega)e^{jn\delta\omega\left(\frac{r}{V_{G_{S_0}}}-t\right)}\right] \tag{4}$$

$$\overline{U}_{A_0}(r,t)\Big|_{\theta_p} = \frac{U_{A_0}}{2n_\omega}e^{j\omega_0\left(\frac{r}{V_{P_{A_0}}}-t\right)}\left[\sum_{n=0}^{n_\omega} g(\omega+n\delta\omega)e^{jn\delta\omega\left(\frac{r}{V_{G_{A_0}}}-t\right)}\right] \tag{5}$$

The individual reconstrutions of the symmetric S_0 and the antisymmetric A_0 modes were superimposed to obtain the full–length reconstructed signal $U_m(r,t)$ along a given propagation direction θ_p.

$$U_m(r,t)\Big|_{\theta_p} = \overline{U}_{S_0}(r,t)\Big|_{\theta_p} + \overline{U}_{A_0}(r,t)\Big|_{\theta_p} + \varepsilon(r,t)\Big|_{\theta_p} \tag{6}$$

The term $\varepsilon(\mathbf{r},t)\big|_{\theta_p}$ denotes the direction-dependent residual error between experimental measurements and the superimposed S_0 and A_0 mode reconstructions. Its mathematical formulation and physical significance are detailed in the following section.

C. Regularized residual error formulation for reconstructed wave parameter estimation

The S_0 and A_0 amplitudes were determined by minimizing the regularized residual error function (RREF). This function was formulated by computing three distinct Euclidean norms.

1) ε_H : Euclidean norm of the difference between the calibrated and experimental Hilbert envelopes [40].
2) ε_{V_P} : Euclidean norm of the difference between the calibrated and semi–analytical phase velocities.
3) ε_{V_G} : Euclidean norm of the difference between the calibrated and semi–analytical group velocities.

The residual error associated with the Hilbert envelope mismatch is given as

$$\varepsilon_H\,(r,t)\,\Big|_{\theta_p} = \sum_{k=1}^{N}\left\|H\left(x^M\right)(t;\Theta) - H(x^e)(t)\right\|_2 \tag{7}$$

Here, N represents the length of the signal in samples, $H(x^e)(t)$ represents the Hilbert analytic envelope of the experimentally measured signal data $x^e(t)$, while $H\left(x^M\right)(t;\Theta)$ represents the Hilbert analytic envelope of the reconstructed ultrasonic signal $x^M(t)$ which depends on the parameter set Θ. Also, we introduce the regularization terms

$$\varepsilon_{V_P}(r,t) = \left\|V_P^{\text{SAFE}} - V_P^M\right\|_2 \quad \text{and} \quad \varepsilon_{V_G}(r,t) = \left\|V_G^{\text{SAFE}} - V_G^M\right\|_2 \tag{8}$$

The L^2 norm in equation 8 highlights the vector-valued phase and group velocities of the fundamental S_0 and A_0 modes, but can be easily generalised to include higher order modes. Therefore, combining equations 7 and 8, we get the expression for the RREF at a specific propagation direction θ_P as

$$\varepsilon(r,t)\Big|_{\theta_p} = \varepsilon_H(r,t)\Big|_{\theta_p} + \boldsymbol{\lambda}^\top \boldsymbol{\varepsilon}_V \quad \text{where} \quad \boldsymbol{\lambda} = \left\{\lambda_{V_P}, \lambda_{V_G}\right\}, \quad \boldsymbol{\varepsilon}_V = \left\{\varepsilon_{V_P}, \varepsilon_{V_G}\right\}. \tag{9}$$

The penalty term $\boldsymbol{\lambda}^\top \boldsymbol{\varepsilon}_V$ helps to regularize the identification of dispersion parameter values while minimizing the error $\varepsilon(r,t)$. The $\lambda_{V_P}, \lambda_{V_G}$ are the weights attached to the phase and group velocity penalty terms respectively. This helped to estimate the S_0 and A_0 modal amplitudes and dispersion characteristics to generate accurate full-length final reconstructions of the experimental signals along multiple propagation directions.

D. Probabilistic Bayesian joint parameter estimation

This section presents a probabilistic–Bayesian joint parameter estimation framework to jointly identify the modal amplitudes and dispersion characteristics, and quantify uncertainties inherent in the identification process. Experimental measurements contain aleatoric uncertainties arising from various noise sources, including measurement noise, human error, amongst others. On the other hand, the semi–analytical dispersion parameters suffer from model form uncertainty due to the idealized assumptions introduced into the model for the sake of keeping the model tractable and the computational overhead manageable. The proposed probabilistic Bayesian approach leverages this complimentary nature by accounting for both the aleatoric uncertainty inherent in the acquired experimental data and the epistemic uncertainty associated with the semi-analytical model predictions. The probabilistic joint parameter estimation considers the parameter set $\Theta = [U_{S_0}, U_{A_0}, V_{P_{S_0}}, V_{P_{A_0}}, V_{G_{S_0}}, V_{G_{A_0}}]$. The prior means for the modal amplitudes U_{S_0} and U_{A_0} are initialized using fixed guess values, while the phase velocities ($V_{P_{S_0}}, V_{P_{A_0}}$) and group velocities ($V_{G_{S_0}}, V_{G_{A_0}}$) derive their priors from semi-analytical model predictions. The likelihood function is based on the direction dependent error function, RREF defined in equation 9 which was minimized along all the propagation directions individually to jointly estimate the parameter set Θ. The Bayesian posterior probabilistic estimate of the modal parameters Θ is given in $\pi\left(\Theta \,\middle|\, H(x^e)(t), \mathcal{M}, \mathrm{d}_{\text{SAFE}}\right)$, which is the joint probabilistic parameter estimate on Θ, conditional on the dispersion data d_{SAFE} and the harmonic wave propagation model $\mathcal{M}$. From Bayes' theorem,

$$\pi\left(\Theta \,\middle|\, H(x^e)(t), \mathcal{M}, \mathrm{d}_{\text{SAFE}}\right) \propto \mathscr{L}\left(H(x^e)(t) \,\middle|\, \Theta, \mathcal{M}\right) \pi\left(\Theta \,\middle|\, \mathrm{d}_{\text{SAFE}}\right) \tag{10}$$

A probabilistic (π) prior is assigned to the dispersion parameter set Θ, expressed as $\pi(\Theta \,|\, \mathrm{d}_{\text{SAFE}})$, conditional on d_{SAFE}, which is the composite waveguide dispersion data from the semi–analytical finite element model for the structure under investigation. Additional regularization of the inverse problem can be achieved by incorporating data from alternative dispersion models or historical datasets. $\mathscr{L}\left(H(x^e)(t) \,\middle|\, \Theta, \mathcal{M}\right)$ is the likelihood of observing the Hilbert envelope of the experimental data $x^e(t)$, conditional on Θ and $\mathcal{M}$. The posterior distribution, estimated as per Equation 10, helps to quantify the uncertainty around the identified parameter values with probabilistic estimates and indicates the robustness of the identified modal parameter values.

IV. Results and discussions

The calibrated wave mode characteristics were used to generate accurate reconstructions of the experimental signals acquired after every 25,000 cycles of displacement–control compressive fatigue loading. In this section, results from wave mode calibration performed on signals acquired prior to fatigue loading, after 75,000 cycles, after 125,000 cycles and after 175,000 cycles along ($0°, 45°, 90°$) propagation directions are presented. Damage was first visible to the naked eye at the top left corner of the sample after approximately 125,000 cycles of fatigue. At this stage, the fatigue test was resumed to progress the damage further. The progression of damage is shown in figure 4. As an initial assessment of the structure's health, the magnitudes of the acquired signals were calculated and shown in figure 5. Along the $0°$ propagation direction, the loss in magnitude was observed between 230kHz–250kHz, with the magnitude largely fluctuating $\pm 1.5\%$

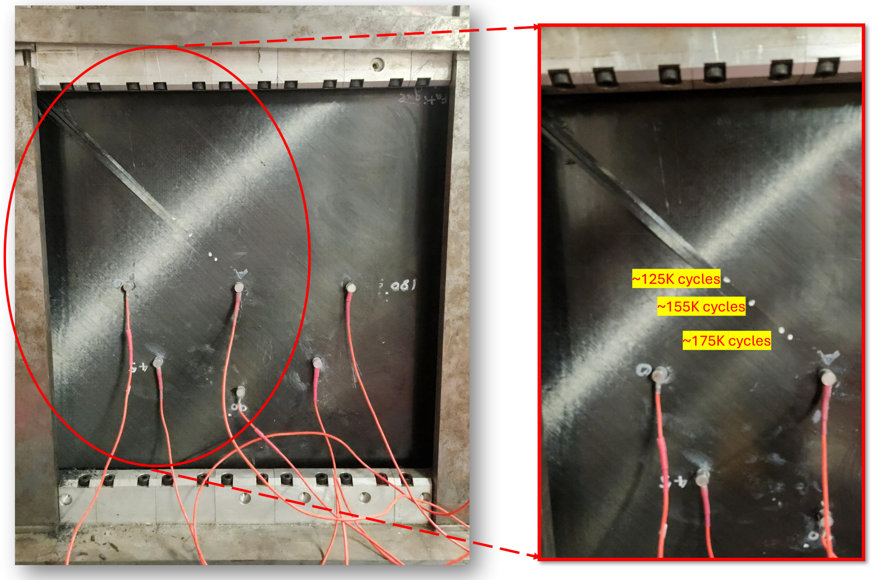

Fig. 4 Damage visible from approx. 125, 000 **cycles of displacement–control compressive fatigue and its progress to approx.** 175, 000 **cycles.**

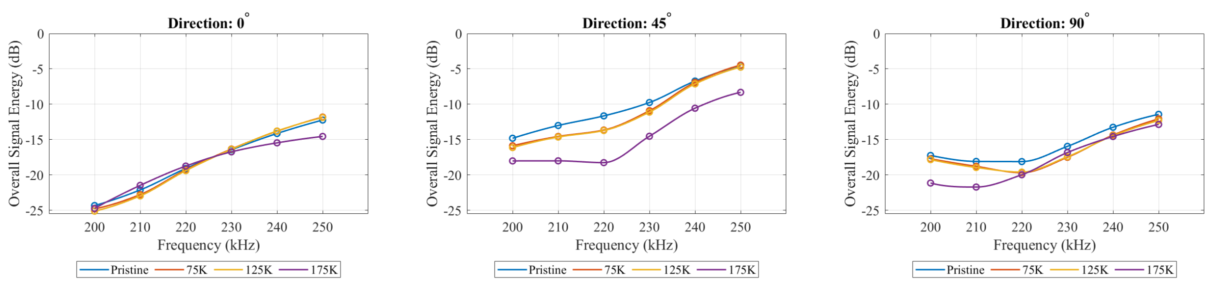

(a) **(b)** **(c)**

Fig. 5 A comparison of overall experimental signal energy characteristics in the frequency range 200**kHz-**250**kHz along** (0°, 45° **and** 90°) **directions at various recorded stages of fatigue.**

about the pristine baseline after 75, 000 and 125, 000 cycles and 8.56% reduction after 175, 000 cycles. Conversely, along the 90° direction, the loss occurred between 200 kHz and 220 kHz, with a reduction of approximately 5% after 75, 000 and 125, 000 cycles, and 17.59% after 175, 000 cycles. A more pronounced degradation was observed along the 45° fiber direction across the frequency band, with magnitude drops of about 10.55%, 12.01%, and a significant 41.64% after 75, 000, 125, 000, and 175, 000 cycles, respectively. To better understand the contributing factors behind the loss in experimental signal magnitudes, the influence of progressive fatigue damage on the fundamental S_0 and A_0 modal characteristics must be investigated, given their established sensitivity to composite damage. This requires first estimating these modal parameters.

An adaptive Metropolis-Hastings Markov Chain Monte Carlo (MH-MCMC) method was implemented to sample from the posterior distribution $\pi\left(\Theta \,\middle|\, H(x^e)(t), \mathcal{M}, \mathrm{d}_{\mathrm{SAFE}}\right)$ of the parameters Θ of observing the experimental data $x^e(t)$, conditional on the modal parameters. The MH-MCMC algorithm generated 10, 000 sets of Θ that fit the posterior. These parameters were used to construct 10, 000 calibrated Hilbert analytic envelopes. The mean posterior Hilbert analytic envelopes and their 90% confidence intervals were overlaid on the experimental signals and presented alongside their corresponding Pearson correlation coefficients (R) and residual errors ε in figure 6. The Pearson coefficient R quantifies the temporal alignment between the recorded and reconstructed signals and the residual error ε measures the absolute magnitude of their discrepancy, together providing a quantitative representation of the reconstruction accuracy. The posterior predictive probabilistic envelopes–corresponding to signals acquired pre–fatigue (pristine baseline), after 75,000 cycles, 125,000 cycles, and 175,000 cycles–demonstrated close agreement with their experimental counterparts across the examined frequency bandwidth as demonstrated by high R and low ε values. The calibrated S_0 and A_0 modal energies with 90% confidence intervals are shown in figure 7 and the calibrated phase and group velocities with 90% confidence intervals are shown in figure 8 and figure 9 respectively.

An interesting feature can be observed in the probabilistic group velocity characteristics–first, consider the estimates between 200kHz–220kHz along 0° and 90° propagation directions. The calibrated S_0 and A_0 group velocities exhibit comparable values with a few instances of coinciding values as well. This observation suggests that the A_0 mode is predominant at this frequency while the S_0 mode amplitude is very low (potentially close to the noise floor). This statement is further reinforced by the waterfall plots that reveal a single wave packet or a low amplitude first wave packet. Considering the estimates between 200kHz–220kHz along the 45° direction, the S_0 probabilistic group velocity exhibits a higher value distinctly separating itself from the A_0 group velocity values consistently across the frequency band. Furthermore, the waterfall plots exhibit two distinct wave packets across the frequency band, clearly establishing that the S_0 mode emerges at a relatively lower frequency of 200kHz along 45°. This trend can be attributed to the laminate's axial stiffness being maximized along the 45° fibre direction, naturally concentrating the guided wave energy along paths of highest effective modulus and least resistance. This leads to higher wave velocities and amplitudes [41], which ultimately causes the emergence of the S_0 mode at a relatively lower frequency in these directions [42].

The probabilistic calibration approach also presents the set of parameters that numerically the most plausible, statistically well–founded and realistically the most likely explanation for the observed data, called the maximum likelihood estimate (MLE). The MLE is the measure of how accurately the probabilistic model can explain the observed experimental signal conditional on $\mathcal{M}$ and Θ. The signals reconstructed using the MLE parameters and their 90% confidence intervals were overlaid on the experimental signals and presented alongside their corresponding Pearson correlation coefficients (R) and residual errors ε in figure 10. Examining the MLE S_0 and A_0 modal energies shown in figure 11 the following observations can be made:

1) As the degradation became more severe, the effects of the damage on both the S_0 and A_0 modes became more pronounced as evidenced by the significant modal energy drop after 175,000 cycles.
2) Progressive degradation was clearly captured by the S_0 and A_0 modal energies along the 45° fiber direction consistently across the chosen frequency band.
3) Along the 0° direction, progressive degradation was captured by both the fundamental modes between 230kHz–250kHz. Conversely along 90°, degradation was only captured by the A_0 mode between 200kHz–220kHz.

To elucidate the individual contributions of guided wave modes to the overall signal characteristics, it is important to examine the trends observed in the individual guided wave mode energies alongside the overall experimental signal energies. For clear visualization, overall signal energy characteristics are displayed together with the individual modal energy characteristics in figure 11. Firstly, consider the 0° propagation direction where the experimental signal energies decreased between 230kHz–250kHz as shown in figure 11a. Within this band, the S_0 modal energy dropped by approximately 42.86%, 66.67%, and 90.48% from the pristine baseline after 75,000, 125,000, and 175,000 fatigue cycles, respectively. The A_0 modal energy exhibited a comparable 40% drop from the pristine baseline after 75,000 and 125,000 cycles and approximately 50% drop after 175,000 cycles. Although both modes exhibit energy reduction due to damage, the S_0 mode more distinctly resolves the progression of fatigue degradation, indicating its greater sensitivity compared to the A_0 mode in the 230–250 kHz band along 0°. This behavior is consistent with the increasing dominance of the S_0 mode at higher frequencies.

Along the 90° propagation direction, the experimental signal energies exhibited a drop between 200kHz–220kHz as shown in figure 11c unlike the trends observed along the 0° propagation direction. The S_0 modal energies only captured the drop after 175,000 cycles of fatigue. On the other hand, the A_0 mode captured a comparable yet a clear drop of 8.82% from the pristine baseline after 75,000 and 125,000 cycles and 32.35% after 175,000 cycles, approximately. This can be attributed to the S_0 mode being less sensitive in this frequency band compared to the A_0 mode. This suggests that the drop observed in the experimental signal energy is largely contributed by the A_0 modal energy characteristics. This is understandable, as the A_0 mode is known to be dominant at lower frequencies in the frequency band considered.

Unlike the trends observed along the 0° and 90° propagation directions, the experimental signal energies exhibited a drop across the entire frequency band along the 45° propagation direction, as shown in figure 11b. The S_0 modal energy characteristics captured the progressive fatigue degradation between 230kHz–250kHz with an approximate 6.5% drop from the pristine baseline after 75,000 cycles, 23.61% after 125,000 cycles and 69.96% after 175,000 cycles of fatigue loading. The A_0 modal energy characteristics were able to capture the distinct stages of fatigue degradation across the

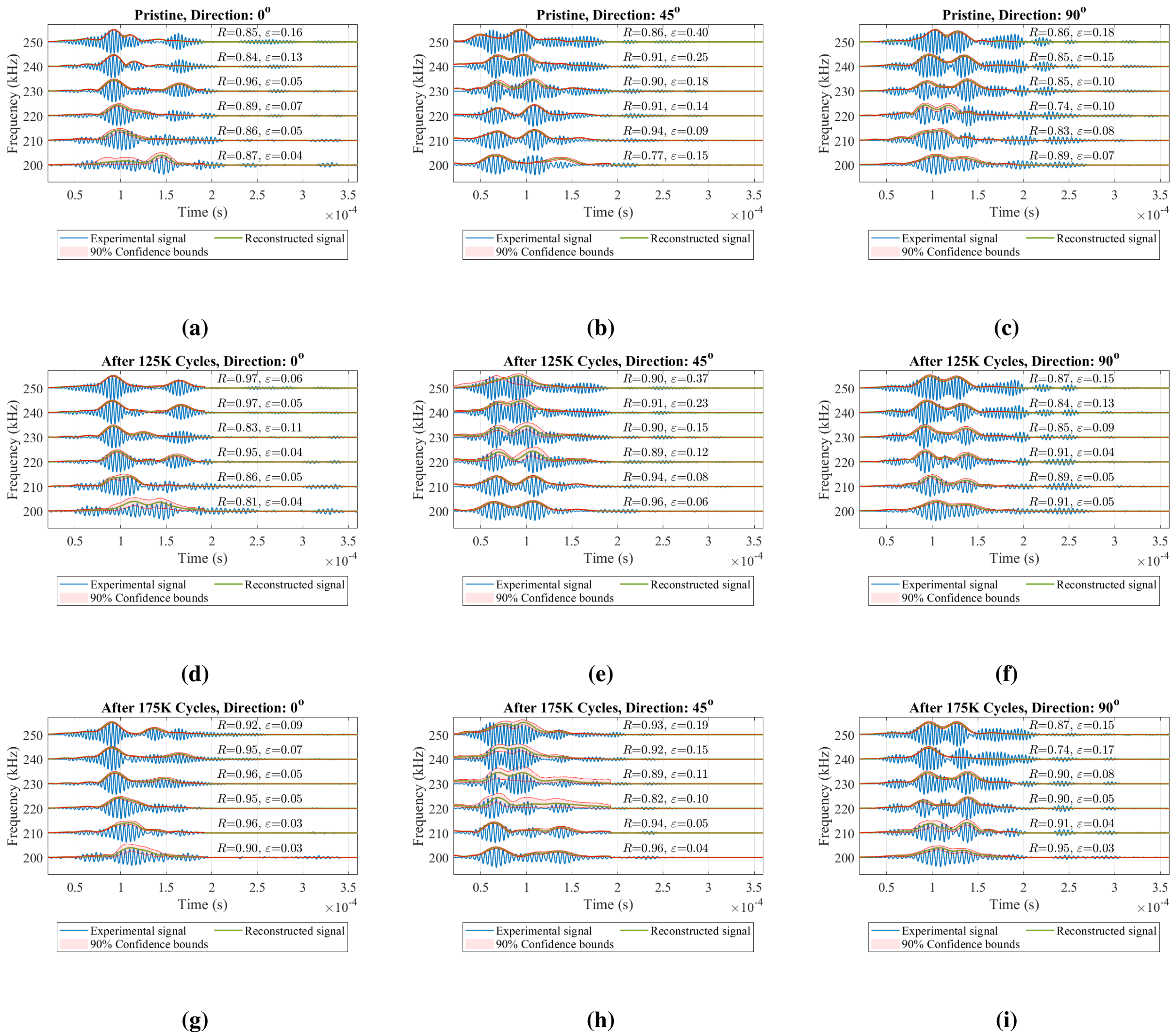

Fig. 6 Physics–informed experimental signal reconstructions derived from probabilistic Bayesian optimization performed along (0°, 45° and 90°) directions at various recorded stages of fatigue. R quantifies the temporal alignment and phase coherence between signals and ε measures the absolute magnitude of their discrepancy, providing a quantitative representation of reconstruction accuracy.

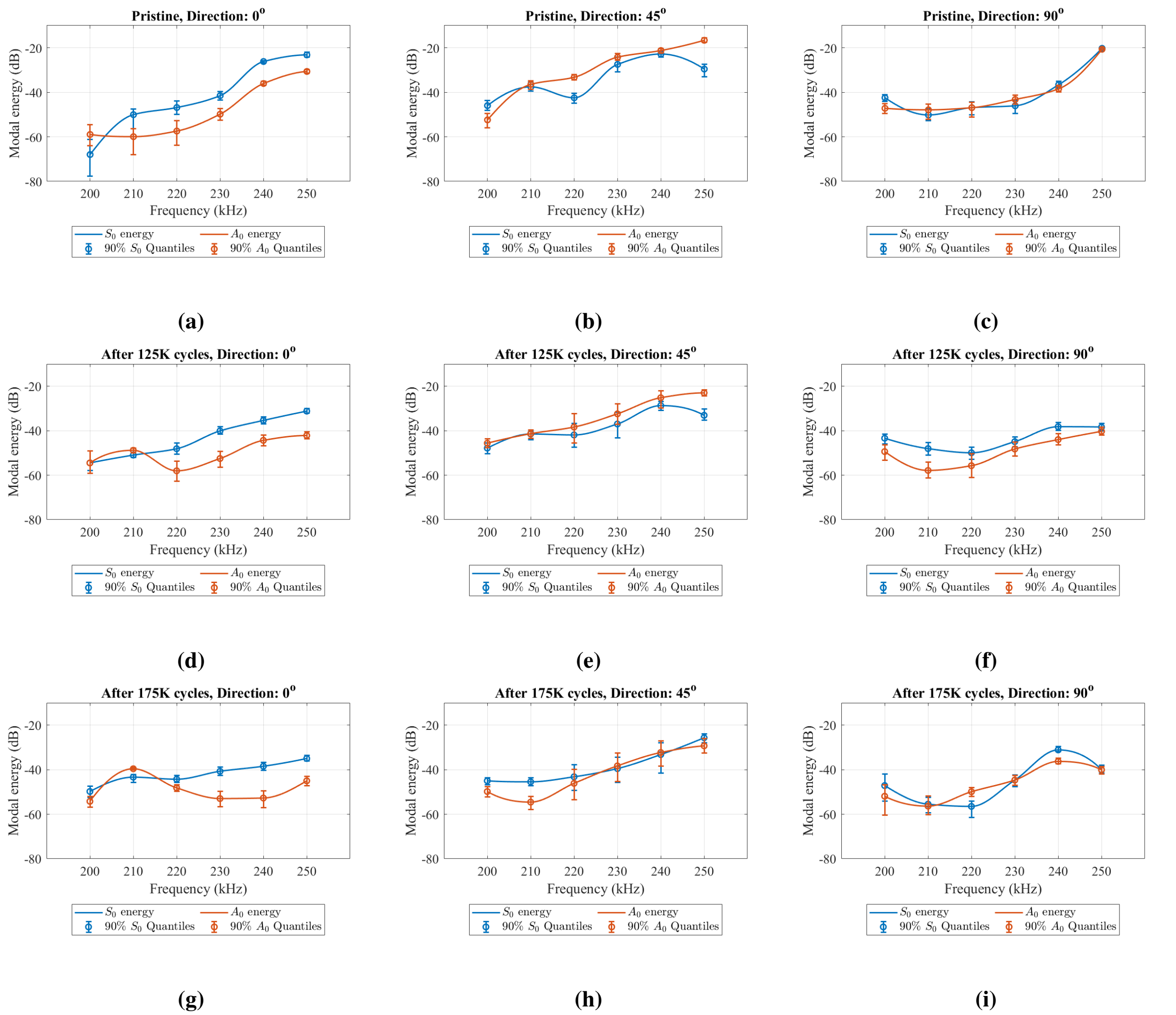

Fig. 7 Semi-analytical model informed and experimental data driven reconstruction of the S_0 and A_0 ultrasonic guided wave modes derived from probabilistic Bayesian optimization performed along $0°$ $45°$, $90°$ propagation directions

entire frequency band under consideration with 24.34% drop from the pristine baseline after 75,000 cycles, 55.96% after 125,000 cycles and 97.97% drop after 175,000 cycles of fatigue loading. This suggests that the A_0 mode is more sensitive to damage along the 45° propagation direction and the major contributing factor behind the energy losses exhibited by the experimental signal energy characteristics.

The probabilistic Bayesian framework has effectively quantified the uncertainty in guided wave parameter estimation, revealing distinct directional and modal sensitivities to various recorded stages of fatigue degradation. The captured individual modal energy characteristics directly explain the trends in the overall experimental signal energy. This establishes the method's capability to not only provide reliable parameter estimates with quantified uncertainty but also to resolve the individual contributions of each guided wave mode to the overall structural response, identifying the most sensitive damage indicators for a given propagation path. Using the proposed methodology, one can

1) Accurately reconstruct the acquired experimental signals at any propagation distance r and angle θ.
2) Capture progressive structural degradation within the individual S_0 and A_0 guided wave modes.
3) Quantify the epistemic and aleatoric uncertainties associated with the parameter estimates.
4) Identify the most probable parameter values that explain the observed data, ensuring the solution remains informed by guided wave physics and grounded in experimental reality.

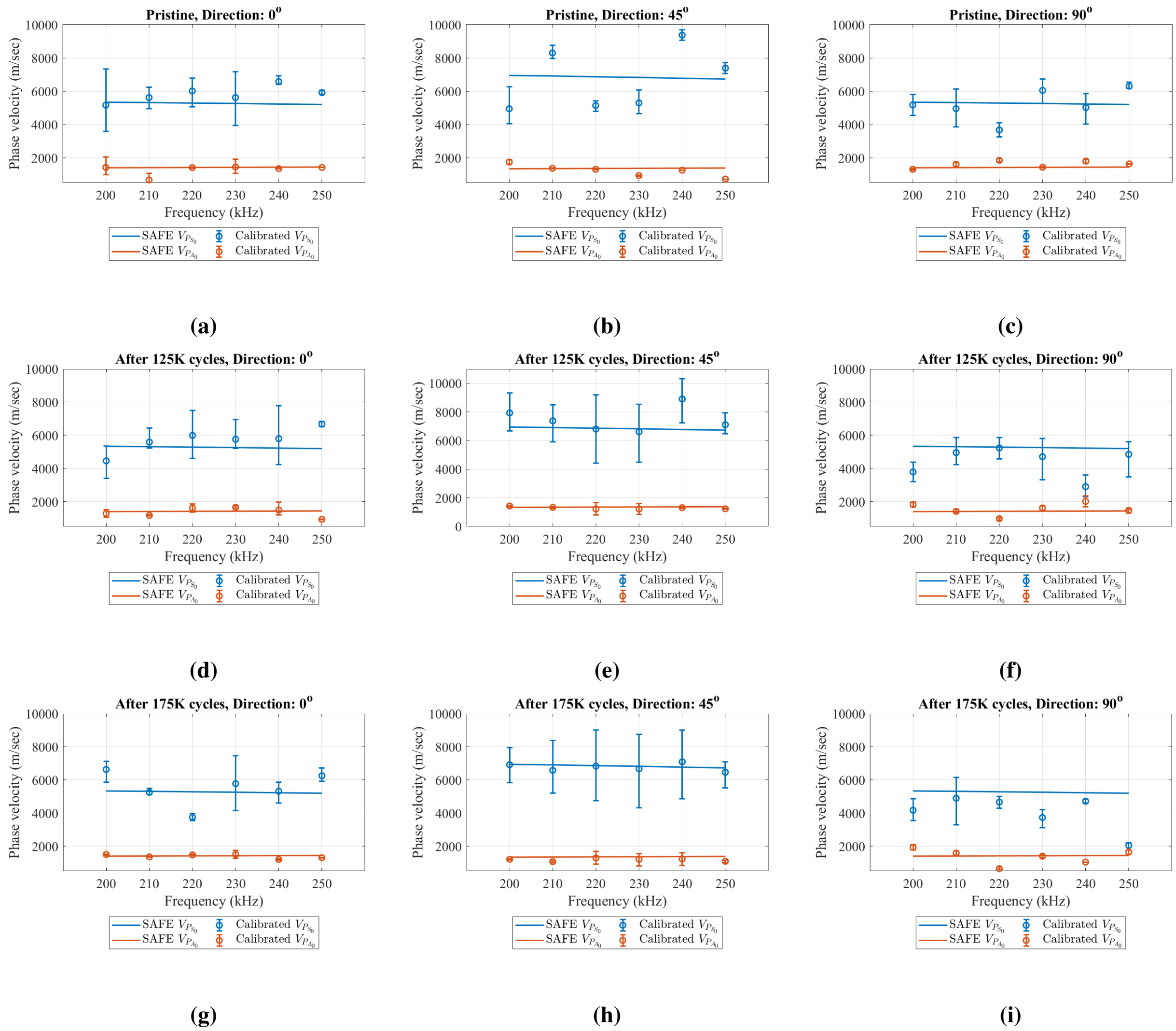

Fig. 8 Semi-analytical and probabilistically calibrated phase velocity values in the frequency range 200kHz-250kHz along (0°, 45° and 90°) directions at various recorded stages of fatigue. (Note: Discrepancies between semi–analytical and calibrated values may exist as the calibrated values combine experimental measurements with semi–analytical predictions to provide an informed estimate of dispersion characteristics)

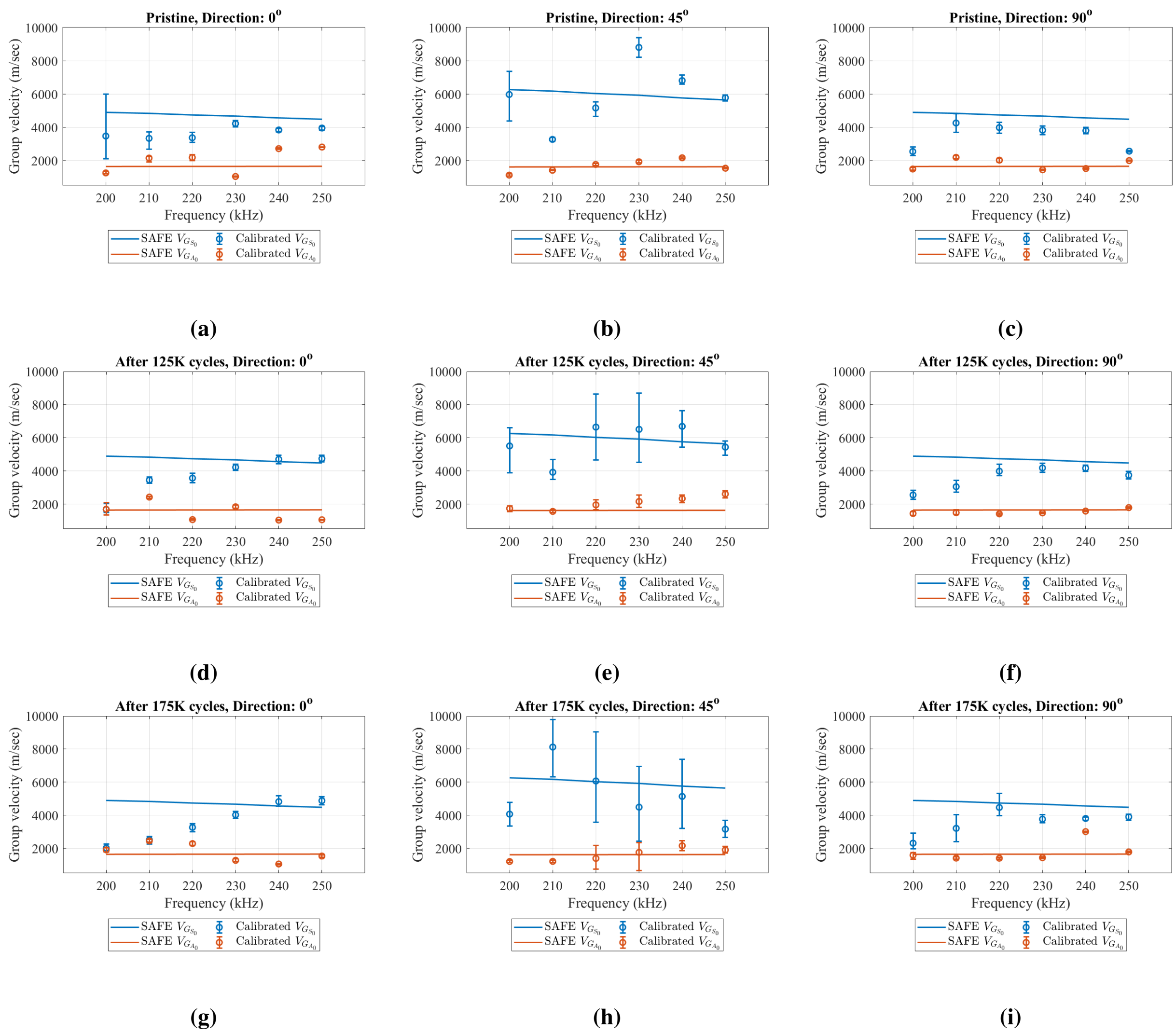

Fig. 9 Semi-analytical and probabilistically calibrated group velocity values in the frequency range 200kHz-250kHz along (0°, 45° and 90°) directions at various recorded stages of fatigue. (Note: Discrepancies between semi–analytical and calibrated values may exist as the calibrated values combine experimental measurements with semi–analytical predictions to provide an informed estimate of dispersion characteristics)

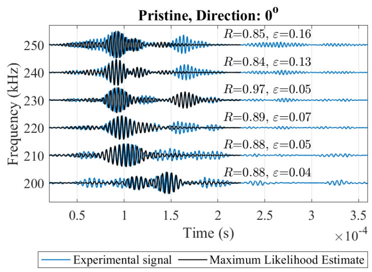

(a)

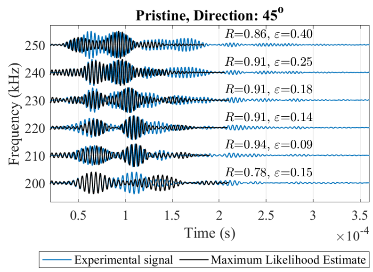

(b)

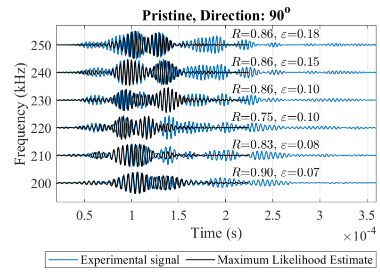

(c)

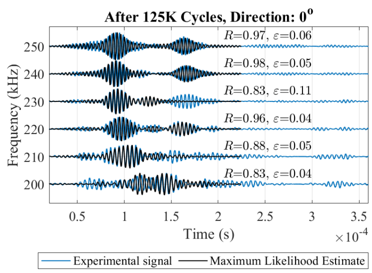

(d)

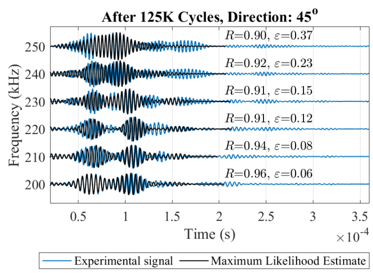

(e)

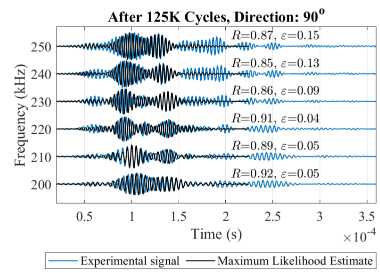

(f)

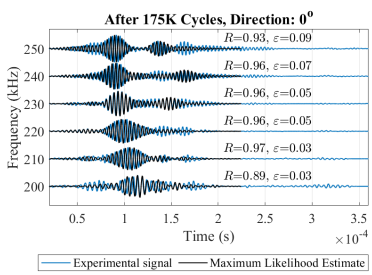

(g)

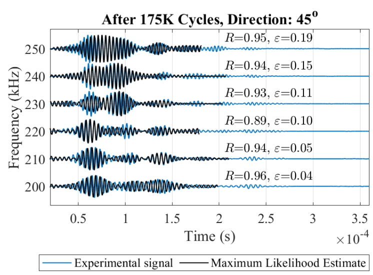

(h)

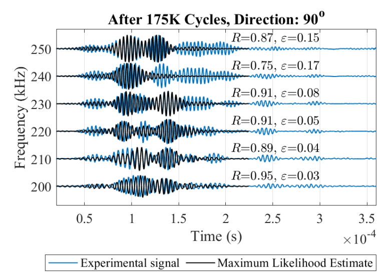

(i)

Fig. 10 Maximum likelihood experimental signal reconstructions derived from probabilistic Bayesian optimization performed along $0°$ $45°$, $90°$ propagation directions at various recorded stages of compressive fatigue. R quantifies the temporal alignment and phase coherence between signals and ε measures the absolute magnitude of their discrepancy, providing a quantitative representation of reconstruction accuracy.

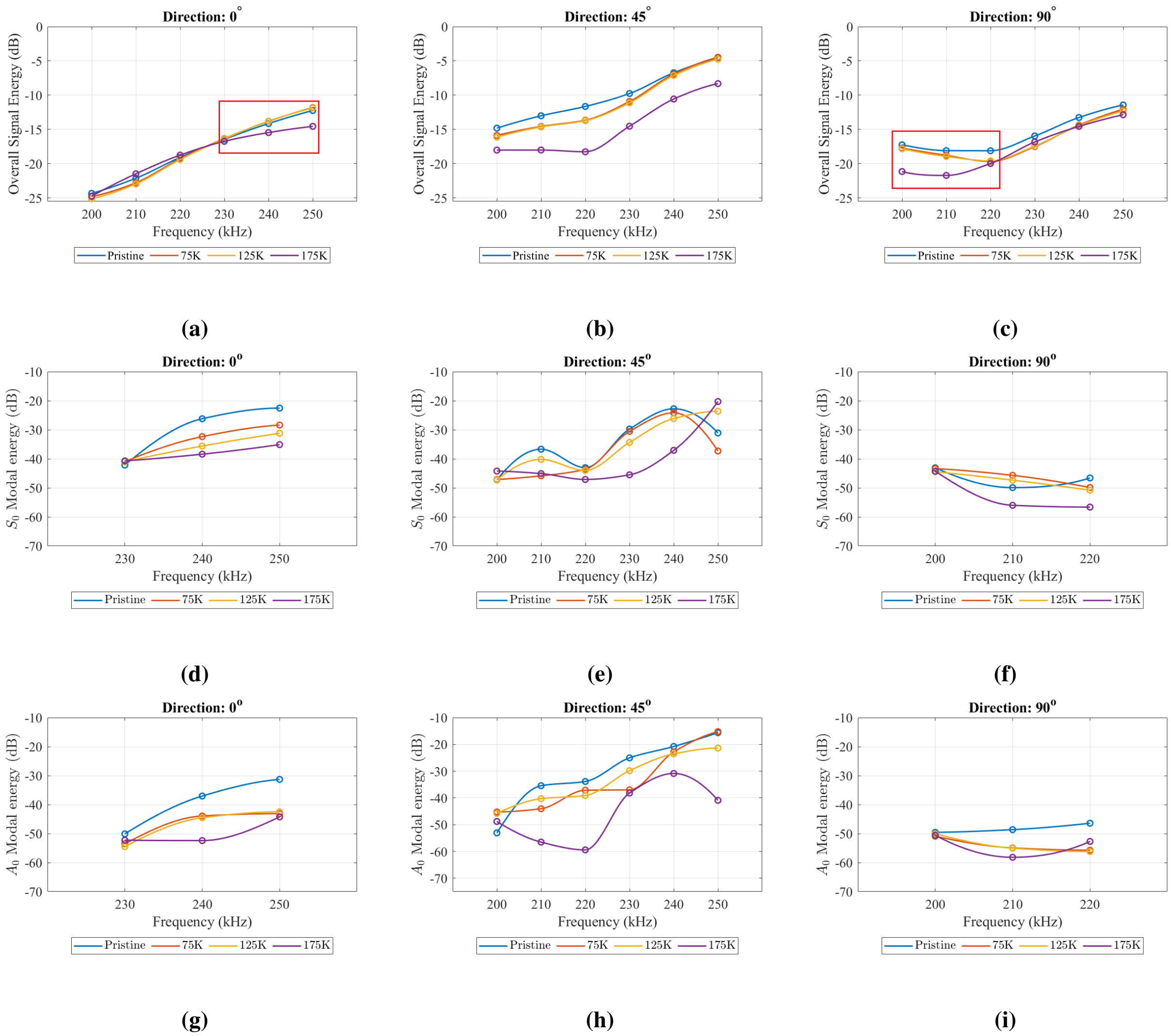

Fig. 11 (figures 11a–11c) are the experimental signal energies re–displayed to be visualized in conjunction with the calibrated maximum likelihood S_0 and A_0 modal energies (figures 11d–11i) derived from probabilistic Bayesian calibration of experimental signals.

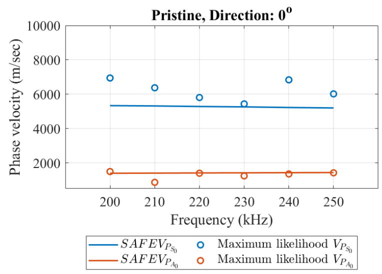

(a)

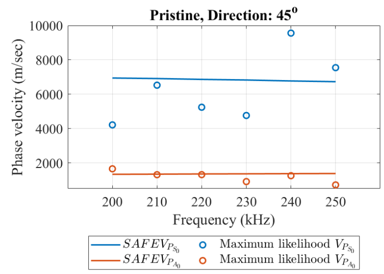

(b)

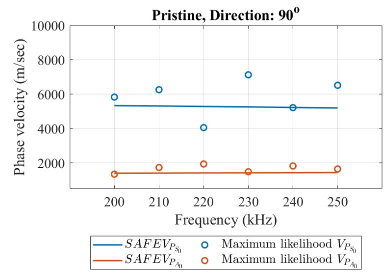

(c)

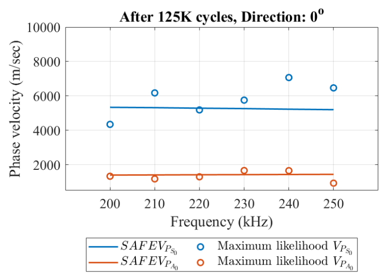

(d)

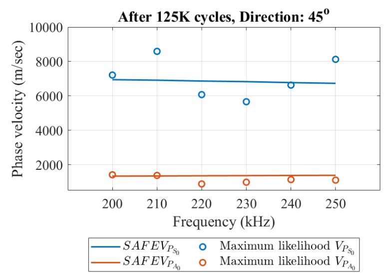

(e)

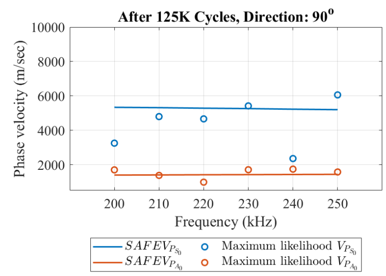

(f)

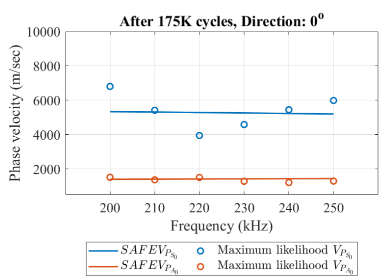

(g)

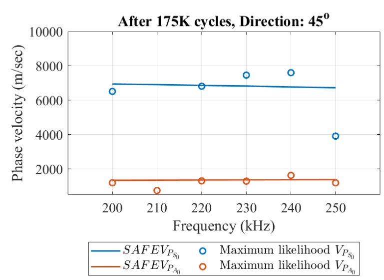

(h)

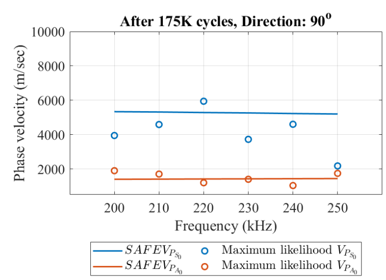

(i)

Fig. 12 Semi-analytical and maximum likelihood phase velocity values in the frequency range 200kHz-250kHz along (0°, 45° and 90°) directions at various recorded stages of fatigue. (Note: Discrepancies between semi–analytical and calibrated values may exist as the calibrated values combine experimental measurements with semi–analytical predictions to provide an informed estimate of dispersion characteristics).

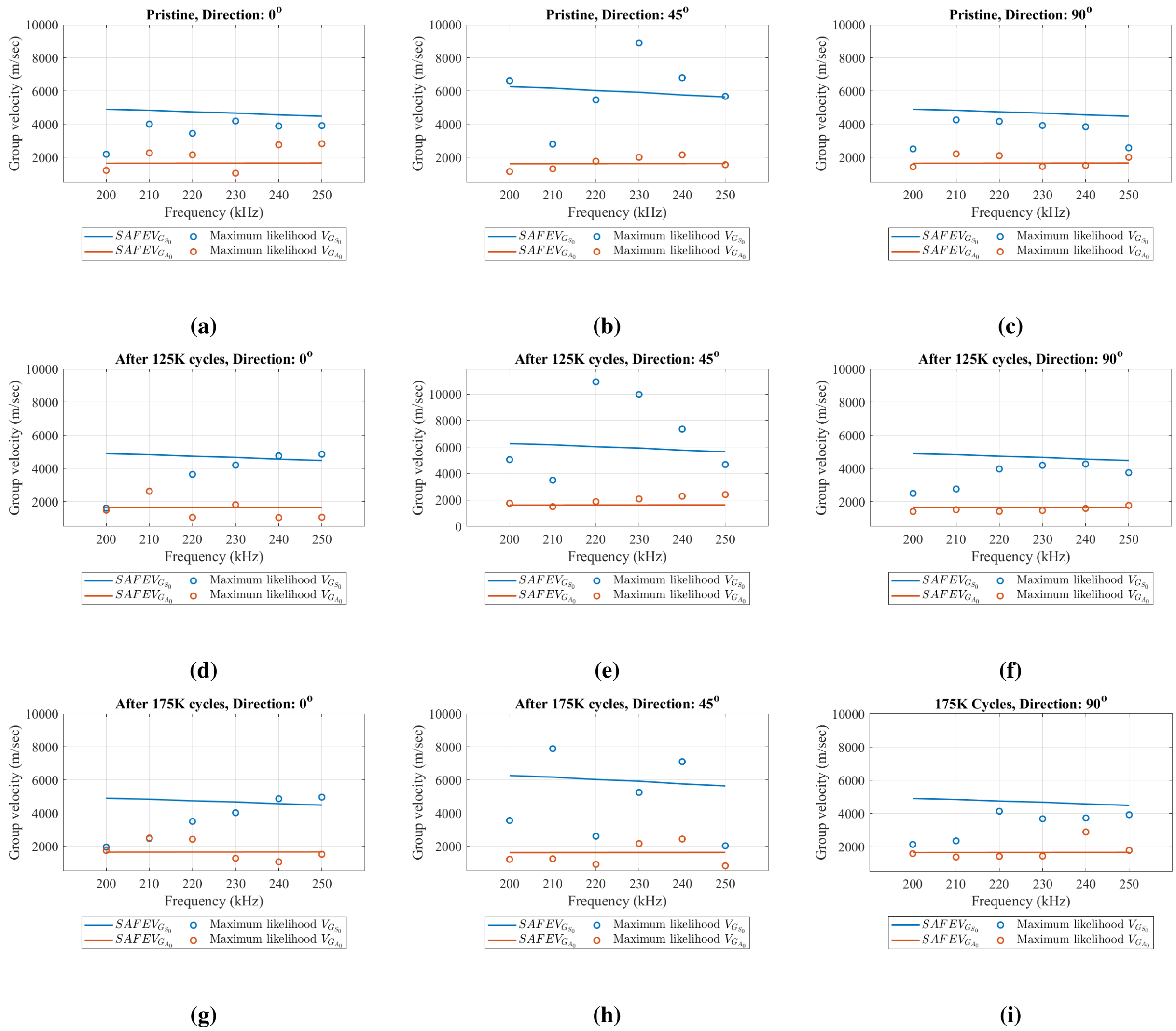

Fig. 13 Semi-analytical and maximum likelihood group velocity values in the frequency range 200kHz-250kHz along (0°, 45° and 90°) directions at various recorded stages of fatigue. (Note: Discrepancies between semi–analytical and calibrated values may exist as the calibrated values combine experimental measurements with semi–analytical predictions to provide an informed estimate of dispersion characteristics).

The proposed physics–informed calibration methodology holds significant potential for practical structural health monitoring by identifying specific monotonic frequencies and propagation directions where particular guided wave modes exhibit peak sensitivity to damage. This capability provides a crucial practical advantage: it allows users to strategically select the most effective combination of actuation frequency/frequency band, propagation direction, and wave mode for a given transducer network to extract essential signal features to capture damage signatures consistently. It is important to note that the results demonstrate the efficacy of the proposed methodology in capturing progressive structural degradation from fatigue loading through calibrated wave mode characteristics, rather than focussing specific damage types. Given the observed sensitivity of specific modal parameters to fatigue-induced damage, future work will introduce controlled damage scenarios such as simulated delaminations, holes, and other stress raisers with known and varying dimensions to establish robust correlations between the captured signatures and parameterized damage metrics.

V. Conclusion

This paper presents a robust, streamlined and reproducible methodology to capture signatures of progressive structural degradation from acquired ultrasonic responses by accurately reconstructing experimental signals at any distance r from the actuator and propagation direction θ_p on thin–walled CFRC structures. Towards this, a parameter set defined by the fundamental S_0 and A_0 mode amplitudes, phase velocities and group velocities was calibrated using a harmonic wave propagation model to generate individual S_0 and A_0 mode realizations and eventually superimposed to produce accurate reconstructions of experimental signals acquired using a semi–circular array of NANO30 piezoelectric transducers. The harmonic wave propagation model is informed by the guided wave physics derived from a semi–analytical composite waveguide and driven by experimental data acquired by a smart edge–computing framework. A regularized residual error function was established to account for discrepancies arising from measurement noise, human error and higher order guided wave modes amongst others. A probabilistic Bayesian methodology was employed to minimize the error and calibrate the wave mode characteristics. The probabilistic Bayesian approach enhanced the reliability of calibration by quantifying the uncertainties associated with the estimates of the individual modal parameters.

The calibrated guided wave mode characteristics successfully captured structural degradation at the various recorded stages of displacement–controlled compressive fatigue loading. The probabilistic Bayesian framework effectively quantified uncertainty in parameter estimation, revealing distinct directional and modal sensitivities to fatigue damage. As the degradation became more severe, the effects of the damage on both modes became more pronounced ,evidenced by severe energy drops emerging after $175,000$ cycles. Progressive degradation was most consistently captured along the 45° fiber direction across the entire frequency band. In other directions, sensitivity was highly mode-dependent: both fundamental modes responded to damage along 0° between 230–250 kHz, whereas only the A_0 mode was effective along 90° between 200–220 kHz. This methodology captures progressive structural degradation within individual guided wave modes at any propagation distance r from the actuator and propagation angle θ_p, and quantifies epistemic and aleatoric uncertainties associated with these estimates. This achievement underscores the efficacy and reliability of the calibrated ultrasonic guided wave modes as reliable identifiers of damage with potential for further description, characterization, and sentencing.

Python scripts containing data acquisition and processing algorithms can be deployed on the CyberSHM smart–edge computing framework employed in this study to enable seamless, single–click functionality to excite any thin–walled structure with user–defined actuation pulses across a specified frequency bandwidth, perform threshold free data acquisition, and wave mode calibration. It is important to note that the results presented in this study showcase the efficacy of the calibrated wave mode characteristics in capturing progressive structural degradation. Future work will focus on extending this methodology by mapping the captured damage signatures to specific damage types and quantitative metrics, while accounting for complex wave interactions such as edge reflections, scattering, and other dissipative mechanisms. Further development includes incorporating additional guided wave modes into the harmonic wave propagation model and validating the calibration framework on complex operational structures beyond simple rectangular panels.

Acknowledgments

This research was funded by Engineering and Physical Sciences Research Council (EPSRC), UK under grant number EP/V055577/1.

References

[1] Wisnom, M., "The role of delamination in failure of fibre-reinforced composites," *Philosophical Transactions of the Royal Society A: Mathematical, Physical and Engineering Sciences*, Vol. 370, No. 1965, 2012, pp. 1850–1870.

[2] Zhang, X., Liu, H.-Y., and Mai, Y.-W., "Effects of fibre debonding and sliding on the fracture behaviour of fibre-reinforced composites," *Composites Part A: applied science and manufacturing*, Vol. 35, No. 11, 2004, pp. 1313–1323.

[3] Beaumont, P., "The failure of fibre composites: an overview," *The Journal of strain analysis for engineering design*, Vol. 24, No. 4, 1989, pp. 189–205.

[4] Nikishkov, Y., Seon, G., and Makeev, A., "Structural analysis of composites with porosity defects based on X-ray computed tomography," *Journal of Composite Materials*, Vol. 48, No. 17, 2014, pp. 2131–2144.

[5] Smith, R., "Composite defects and their detection," *Materials science and engineering*, Vol. 3, No. 1, 2009, pp. 103–143.

[6] Zimmermann, N., and Wang, P. H., "A review of failure modes and fracture analysis of aircraft composite materials," *Engineering failure analysis*, Vol. 115, 2020, p. 104692.

[7] Singh, T., and Sehgal, S., "Structural health monitoring of composite materials," *Archives of Computational Methods in Engineering*, Vol. 29, No. 4, 2022, pp. 1997–2017.

[8] Liu, X., Bai, C., Xi, X., Zhou, S., Zhang, X., Li, X., Ren, Y., Yang, J., and Yang, X., "Impact response and crashworthy design of composite fuselage structures: An overview," *Progress in Aerospace Sciences*, 2024, p. 101002.

[9] Hu, C., Xu, Z., Huang, M., Cai, C., Wang, R., and He, X., "An insight into the mechanical behavior and failure mechanisms of T-stiffened composite structures with through-interface debonding defects," *Ocean Engineering*, Vol. 300, 2024, p. 117342.

[10] Aktan, E., Bartoli, I., Glišić, B., and Rainieri, C., "Lessons from Bridge Structural Health Monitoring (SHM) and Their Implications for the Development of Cyber-Physical Systems," *Infrastructures*, Vol. 9, No. 2, 2024, p. 30.

[11] Dhiman, B., Guleria, V., and Sharma, P., "Applications and future trends of carbon fiber reinforced polymer composites: a review," *International Research Journal of Engineering and Technology*, Vol. 7, No. 10, 2020, pp. 1–7.

[12] Gupta, M., Singhal, V., and Rajput, N., "Applications and Challenges of Carbon-fibres reinforced Composites: A Review," *Evergreen*, Vol. 9, 2022, p. 682. https://doi.org/10.5109/4843099.

[13] Scott, M. J., Verhagen, W. J. C., Bieber, M. T., and Marzocca, P., "A Systematic Literature Review of Predictive Maintenance for Defence Fixed-Wing Aircraft Sustainment and Operations," *Sensors*, Vol. 22, No. 18, 2022. https://doi.org/10.3390/s22187070, URL https://www.mdpi.com/1424-8220/22/18/7070.

[14] Lu, H., Chandran, B., Wu, W., Ninic, J., Gryllias, K., and Chronopoulos, D., "Damage features for structural health monitoring based on ultrasonic Lamb waves: Evaluation criteria, survey of recent work and outlook," *Measurement*, 2024, p. 114666.

[15] Guo, N., and Cawley, P., "The interaction of Lamb waves with delaminations in composite laminates," *The Journal of the Acoustical Society of America*, Vol. 94, No. 4, 1993, pp. 2240–2246. https://doi.org/10.1121/1.407495, URL https://doi.org/10.1121/1.407495.

[16] Aslam, M., Park, J., and Lee, J., "A comprehensive study on guided wave dispersion in complex structures," *International Journal of Mechanical Sciences*, Vol. 269, 2024, p. 109089.

[17] Mei, H., James, R., Haider, M. F., and Giurgiutiu, V., "Multimode Guided Wave Detection for Various Composite Damage Types," *Applied Sciences*, Vol. 10, 2020, p. 484. URL https://api.semanticscholar.org/CorpusID:210941385.

[18] Dafydd, I., and Khodaei, Z. S., "Damage severity assessment in composite structures using ultrasonic guided waves with chirp excitation," *Smart Structures and Materials + Nondestructive Evaluation and Health Monitoring*, 2018. URL https://api.semanticscholar.org/CorpusID:139335731.

[19] Mei, H., Haider, M. F., James, R., and Giurgiutiu, V., "Pure S0 and SH0 detections of various damage types in aerospace composites," *Composites Part B-engineering*, Vol. 189, 2020, p. 107906. URL https://api.semanticscholar.org/CorpusID:213695946.

[20] Yan, G., Lu, X., and Tang, J., "Guided Wave-Based Monitoring of Evolution of Fatigue Damage in Glass Fiber/Epoxy Composites," *Applied Sciences*, 2019. URL https://api.semanticscholar.org/CorpusID:109936309.

[21] Amjad, U., Yadav, S. K., and Kundu, T., "Detection and quantification of pipe damage from change in time of flight and phase," *Ultrasonics*, Vol. 62, 2015, pp. 223–236. https://doi.org/https://doi.org/10.1016/j.ultras.2015.05.022, URL https://www.sciencedirect.com/science/article/pii/S0041624X15001419.

[22] Qatu, K. M., Abdelgawad, A., and Yelamarthi, K., "Structure damage localization using a reliable wave damage detection technique," *2016 International Conference on Electrical, Electronics, and Optimization Techniques (ICEEOT)*, 2016, pp. 1959–1962. https://doi.org/10.1109/ICEEOT.2016.7755031.

[23] Leong, W., Staszewski, W. J., Lee, B., and Scarpa, F., "Structural health monitoring using scanning laser vibrometry: III. Lamb waves for fatiguecrack detection," *Smart Materials and Structures*, Vol. 14, No. 6, 2005, p. 1387.

[24] Lee, B., and Staszewski, W., "Lamb wave propagation modelling for damage detection: II. Damage monitoringstrategy," *Smart materials and structures*, Vol. 16, No. 2, 2007, p. 260.

[25] Su, Z., and Ye, L., *Identification of damage using Lamb waves: from fundamentals to applications*, Vol. 48, Springer Science & Business Media, 2009.

[26] Gullapalli, A., Aburakhis, T., Featherston, C., Pullin, R., Morini, L., and Kundu, A., "A cyberphysical structural health monitoring framework for threshold-free active signal detection and classification on the edge," *Journal of Nondestructive Evaluation, Diagnostics and Prognostics of Engineering Systems*, 2024, pp. 1–14. https://doi.org/10.1115/1.4066196.

[27] Wu, W., Malik, M., Cantero-Chinchilla, S., Lawrie, T., Yan, W., Tanner, G., Remenyte-Prescott, R., and Chronopoulos, D., "Guided waves-based damage identification in plates through an inverse Bayesian process," *Ultrasonics*, Vol. 125, 2022, p. 106773.

[28] Abbas, M., and Shafiee, M., "Structural health monitoring (SHM) and determination of surface defects in large metallic structures using ultrasonic guided waves," *Sensors*, Vol. 18, No. 11, 2018, p. 3958.

[29] Olisa, S. C., Khan, M. A., and Starr, A., "Review of current guided wave ultrasonic testing (GWUT) limitations and future directions," *Sensors*, Vol. 21, No. 3, 2021, p. 811.

[30] Ngo, N. K., Nguyen, T. Q., Vu, T. V., and Nguyen-Xuan, H., "An fast Fourier transform–based correlation coefficient approach for structural damage diagnosis," *Structural Health Monitoring*, Vol. 20, No. 5, 2021, pp. 2360–2375. https://doi.org/10.1177/1475921720949561, URL https://doi.org/10.1177/1475921720949561.

[31] Law, S., Li, X., and Lu, Z., "Structural damage detection from wavelet coefficient sensitivity with model errors," *Journal of engineering mechanics*, Vol. 132, No. 10, 2006, pp. 1077–1087.

[32] Paget, C. A., Grondel, S. b., Levin, K., and Delebarre, C., "Damage assessment in composites by Lamb waves and wavelet coefficients," *Smart materials and structures*, Vol. 12, No. 3, 2003-06-01.

[33] Niethammer, M., Jacobs, L. J., Qu, J., and Jarzynski, J., "Time-frequency representations of Lamb waves," *The Journal of the Acoustical Society of America*, Vol. 109, No. 5, 2001, pp. 1841–1847.

[34] Zhang, C., Mousavi, A. A., Masri, S. F., and Gholipour, G., "The State-of-the-Art on Time-Frequency Signal Processing Techniques for High-Resolution Representation of Nonlinear Systems in Engineering," *Archives of Computational Methods in Engineering*, 2024, pp. 1–22.

[35] Liu, Z., Xu, K., Li, D., Ta, D., and Wang, W., "Automatic mode extraction of ultrasonic guided waves using synchrosqueezed wavelet transform," *Ultrasonics*, Vol. 99, 2019, p. 105948. https://doi.org/https://doi.org/10.1016/j.ultras.2019.105948, URL https://www.sciencedirect.com/science/article/pii/S0041624X19300034.

[36] Huang, N. E., Shen, Z., Long, S. R., Wu, M. C., Shih, H. H., Zheng, Q., Yen, N.-C., Tung, C. C., and Liu, H. H., "The empirical mode decomposition and the Hilbert spectrum for nonlinear and non-stationary time series analysis," *Proceedings of the Royal Society of London. Series A: mathematical, physical and engineering sciences*, Vol. 454, No. 1971, 1998, pp. 903–995.

[37] Gullapalli, A., Aburakhis, T., Featherston, C., Pullin, R., and Kundu, A., "A Model-Informed Approach to Robust Calibration of Experimental Guided Wave Modes with Cyberphysical Systems," *AIAA SCITECH 2025 Forum*, 2025, p. 1219.

[38] Gullapalli, A., Aburakhis, T., Featherston, C., Pullin, R., Morini, L., and Kundu, A., "A cyberphysical structural health monitoring framework for threshold-free active signal detection and classification on the edge," *Journal of Nondestructive Evaluation, Diagnostics and Prognostics of Engineering Systems*, Vol. 8, No. 2, 2025.

[39] Eaton, M., *Acoustic emission (AE) monitoring of buckling and failure in carbon fibre composite structures*, Cardiff University (United Kingdom), 2007.

[40] Klingspor, M., “Hilbert transform: Mathematical theory and applications to signal processing,” , 2015.

[41] Hervin, F. L., “Guided wave propagation and scattering in anisotropic composite structures,” Ph.D. thesis, UCL (University College London), 2023.

[42] Hervin, F., and Fromme, P., “Anisotropy influence on guided wave scattering for composite structure monitoring,” *Structural Health Monitoring*, Vol. 22, No. 4, 2023, pp. 2626–2640. https://doi.org/10.1177/14759217221133284, URL https://doi.org/10.1177/14759217221133284.